SOFT ROBOTS

Electrostatic footpads enable agile insect-scale soft robots with trajectory control

Jiaming Liang[1,2,3†], Yichuan Wu[4†], Justin K. Yim[5], Huimin Chen[3], Zicong Miao[3], Hanxiao Liu[1,3], Ying Liu[1], Yixin Liu[3], Dongkai Wang[1,2,3], Wenying Qiu[1,2,3], Zhichun Shao[2], Min Zhang[3]*, Xiaohao Wang[1,3], Junwen Zhong[2,6]*, Liwei Lin[1,2]*

Agility and trajectory control are two desirable features for robotics, but they become very challenging for soft robots without rigid structures to support rapid manipulations. Here, a curved piezoelectric thin film driven at its structural resonant frequency is used as the main body of an insect-scale soft robot for its fast translational movements, and two electrostatic footpads are used for its swift rotational motions. These two schemes are simultaneously executed during operations through a simple two-wire connection arrangement. A high relative centripetal acceleration of 28 body length per square second compared with existing robots is realized on a 65-milligram tethered prototype, which is better than those of common insects, including the cockroach. The trajectory manipulation demonstration is accomplished by navigating the robot to pass through a 120-centimeter-long track in a maze within 5.6 seconds. One potential application is presented by carrying a 180-milligram on-board sensor to record a gas concentration route map and to identify the location of the leakage source. The radically simplified analog motion adjustment technique enables the scale-up construction of a 240-milligram untethered robot. Equipped with a payload of 1660 milligrams to include the control circuit, a battery, and photoresistors, the untethered prototype can follow a designated, 27.9-centimeter-long "S"-shaped path in 36.9 seconds. These results validate key performance attributes in achieving both high mobility and agility to emulate living agile insects for the advancements of soft robots.

INTRODUCTION

Both agility and trajectory manipulation are important features for practical robots. Specifically, fast-running robots without the ability to navigate around obstacles by coordinating both speedy translational and rotational motions would not be able to execute even common tasks in complex environments. These two desirable characteristics become even more challenging for soft robots due to their unique structural constraints of high flexibility, deformability (*1*, *2*), and robustness (*3*, *4*). For example, conventional rigid-body robots can use differential gaits to realize turning motions similar to those in insects (*5*–*10*). However, soft robots have difficulty using this strategy due to their low structural stiffness, which reduces their ability to manage good motion controls (*3*, *11*–*14*). Previously, trajectory manipulations of robots on the basis of pneumatic structures with the body length scale of more than 10 cm have been demonstrated with relatively poor agility due to their slow moving speeds (*14*–*17*). An insect-scale soft robot has achieved high moving speeds up to 20 body length/s (BL/s) by its unique structural design and driving scheme, but it has exhibited low agility and poor trajectory controllability (*18*). Some insect-scale soft robots on the basis of dielectric elastomer actuators have been developed to show various moving trajectory patterns by advanced digital control schemes (*19*–*22*). However, a key fundamental challenge in the field of insect-scale soft robots is the ultrahigh agility and good trajectory control that are comparable to those of real agile insects. One application scenario for such a robot is to move quickly similar to a cockroach by carrying sensors in ruins after disastrous events and to record and transmit valuable information in search and rescue operations. Bio-inspired soft robots having the advantages of flexibility, deformability, and robustness are desirable for these applications, but their soft bodies often result in poor agility, which limits their functions.

The difficulty in achieving high agility of any robot is to have a very fast linear moving speed while maintaining the capability of making turns. Specifically, a fast-moving robot could lose its stability while executing the turning motions due to the inertia effect. In nature, insects having flexible bodies can dynamically tune the friction force with secretions between their feet and the ground to improve locomotion (*23*–*27*). Similar schemes have been emulated in small-scale robots to accomplish various exceptional functions, such as climbing on a vertical wall using the electrostatic force for attachments (*7*, *19*). Inspired by this strategy, a tethered prototype soft robot has been built by using a curved unimorph piezoelectric film structure as the main body for fast moving speeds, and two electrostatic footpads have been implemented for speedy turning motions. The friction force between the electrostatic footpads and the ground can be independently adjusted by varying the footpads DC bias voltages to regulate the moving trajectory. Key advancements of this work include (i) the highest relative centripetal acceleration among robots at 28 BL/s^2 for a 3 cm–by–1.5 cm, 65-mg tethered prototype with highly robust operations; (ii) a trajectory manipulation demonstration of a tethered robot to navigate through a 120-cm-long path in a maze in just 5.6 s and an application presentation by carrying a 180-mg gas sensor to detect gas leakages; and (iii) a 2.4 cm–by–2.2 cm, 240-mg untethered robot with light-induced motion adjustment controls by carrying a 6.9 times heavier

[1]Tsinghua-Berkeley Shenzhen Institute, Tsinghua University, Shenzhen 518055, China. [2]Berkeley Sensor and Actuator Center, Department of Mechanical Engineering, University of California at Berkeley, Berkeley, CA 94720, USA. [3]Tsinghua Shenzhen International Graduate School, Tsinghua University, Shenzhen 518055, China. [4]School of Mechanical and Electrical Engineering, University of Electronic Science and Technology of China, Chengdu 611731, China. [5]Department of Mechanical Engineering, Carnegie Mellon University, Pittsburgh, PA 15289, USA. [6]Department of Electromechanical Engineering, Centre for Artificial Intelligence and Robotics, University of Macau, Macao 999078, China.
*Corresponding author. Email: zhang.min@sz.tsinghua.edu.cn (M.Z.); junwenzhong@um.edu.mo (J.Z.); lwlin@berkeley.edu (L.L.)
†These authors contributed equally to this work.

payload (1.66 g, including a battery, photoresistors, and control circuit) to finish a designated, 27.9-cm long "S"-shaped path in 36.9 s. In this case, a simplified, two-wire motion adjustment technique enables the easy setup of power electronics for the scale-up untethered robot. The design principles, motion manipulation methodologies, system characterizations, and application demonstrations all aim to advance the field of soft robots with the goal to emulate agile insects toward practical applications.

RESULTS

Design strategy and basic mechanism

An optical image of a tethered, insect-scale soft robot (3 cm by 1.5 cm, 65 mg) is shown in Fig. 1A together with a queen ant (*Camponotus turkestanus*) for size comparison. The fabrication processes are given in Materials and Methods on the basis of the previous work (*18*) with added electrostatic footpads. The robot is composed of a main body, a rear leg, and two front legs with electrostatic footpads. The scanning electron microscopy (SEM) image in Fig. 1B shows the cross-sectional view of the main body made of three polymer layers: the curve-shaped piezoelectric polyvinylidene fluoride (PVDF; 18-μm) thin film with top and bottom titanium (Ti)/gold (Au) (10/100 nm) electrodes, the silicone adhesive layer (25 μm), and the polyethylene terephthalate (PET; 25-μm) passive layer at the bottom. Under the excitation of an AC driving voltage at the structural resonant frequency (113 to 190 Hz for the prototypes with slightly different design and fabrication variations), the curved piezoelectric unimorph structure can extend and shrink repeatedly to result in the rear leg and the two front legs striking the ground for fast forward movements (fig. S1). The electrostatic front footpad has the design shape of a droplet and is made of a polyimide (PI; 5 μm in thickness) film at the bottom with a Ti/Au (10/100 nm) electrode on the top. The total footpad area is 32 mm^2, as shown in Fig. 1C. A PET frame is attached on top of the footpad with the help of silicone adhesive as the mechanical support. The electrodes of the right and left footpads are connected to the bottom and top electrodes of the piezoelectric unimorph robot body, respectively. The droplet-shaped design is helpful to enlarge the contact area between the footpad and the ground surface with little impact on the linear moving speed. The front leg is 4 mm in height and is composed of PET/silicone/electrode/PI. The rear leg is a piece of PET film attached to the tail of the robot's main body, with a height of 3.5 mm.

In nature, an ant can change the friction force with the ground by secretion, as shown in Fig. 1D, to help its locomotion on smooth or vertical surfaces (*28*). The agility of the soft robot can be markedly improved by adding two electrostatic footpads to adjust its friction force (f_{shear}), as shown in Fig. 1E as

$$f_{shear} = \mu_0(F_{ad} + F_n) \quad (1)$$

where μ_0 is the friction coefficient between the footpad and the substrate; F_n is the normal force, which is small due to the light weight of the soft robot; and F_{ad} is the electrostatic force generated by the applied electrical field, E, on the footpad as

$$F_{ad} = \frac{1}{2}A\varepsilon_0\varepsilon_r E^2 \quad (2)$$

where A is the contact area between the footpad and ground, ε_0 is the vacuum permittivity, and ε_r is the relative permittivity of the medium between the footpad electrode and ground (mainly the PI film). The friction force between an electrostatic footpad and three different substrates—paper (printer paper, 80 g/m^2; no. 7378, Deli Inc.), polymer (frosted polyvinyl chloride, Foojo Inc.), and metal (InSnBi alloy, Dingguan Inc.)—under applied DC bias voltages from −250 to 250 V have been characterized with the setup in fig. S2A and summarized in Fig. 1F. The friction force increases symmetrically with respect to the positive and negative DC voltages and proportionally to the square of the applied voltage as predicted in Eq. 2. The friction force has its maximum value of ±0.9 mN on the metal substrate (slightly lower at ±0.6 mN for the paper and polymer substrates) under an applied footpad DC bias voltage of ±250 V. Furthermore, the high surface roughness of the polymer substrate as compared with those of the other two substrates (fig. S2, C to E) contributes to its relatively high friction force under the zero DC bias voltage.

By adjusting the friction force between the right and left electrostatic footpads, the robot can produce movements with adjustable trajectories, including straight, clockwise, and counterclockwise motions. For example, the motion of a prototype robot was adjusted to realize the "L" and "3" trajectory paths on a paper substrate in 1.2 and 1.6 s, respectively. By driving at its resonant frequency of 143 Hz for fast moving speeds with agile rotational turning capability in Fig. 1G, the tethered robot achieved a moving speed of 7.81 BL/s and a turning rate of 482°/s, respectively, in these two separated tests.

In general, both small size and light weight could help increase the agility of the robot. The effective friction coefficient gradient $\Delta\mu/\mu_o$ under an applied voltage on the footpad can be derived as

$$\frac{\Delta\mu}{\mu_0} = \frac{\Delta f}{f_0} = \frac{F_{ad}}{mg\mu_0} = \frac{A\varepsilon_0\varepsilon_r E^2}{2mg\mu_0} \quad (3)$$

where $\Delta\mu$ is the difference of friction coefficients before and after an external voltage is applied on the footpad, g is the gravitational constant, and m is the mass of the robot. A high gradient value, which is proportional to the electrostatic adhesion force and inversely proportional to the mass, implies that the robot can easily make a turning motion. As such, a large applied voltage together with a low body mass can increase the agility.

Trajectory control strategy

Figure 2A shows the schematic diagram of the locomotion adjustment scheme with three key elements: the signal generation module, amplifier module, and robot. Two 180° phase-coupled AC square waves sharing the same ground reference were applied to (i) the bottom electrode of the main body and the right electrostatic footpad and (ii) the top electrode of the main body and the left electrostatic footpad, respectively. The AC voltage inputs match the resonant frequency of the prototype robots to result in high moving speeds (*18*). The rotational motion adjustment was achieved by tuning the DC bias voltages to adjust the left and right friction forces, f_{sl} and f_{sr}, on the footpads as

$$f_{sl} = \mu_0\left(\frac{1}{2}A\varepsilon_0\varepsilon_r(E_{drive}(t)+E_{bias}(t))^2 + F_n\right) \quad (4)$$

$$f_{sr} = \mu_0\left(\frac{1}{2}A\varepsilon_0\varepsilon_r(E_{drive}(t)-E_{bias}(t))^2 + F_n\right) \quad (5)$$

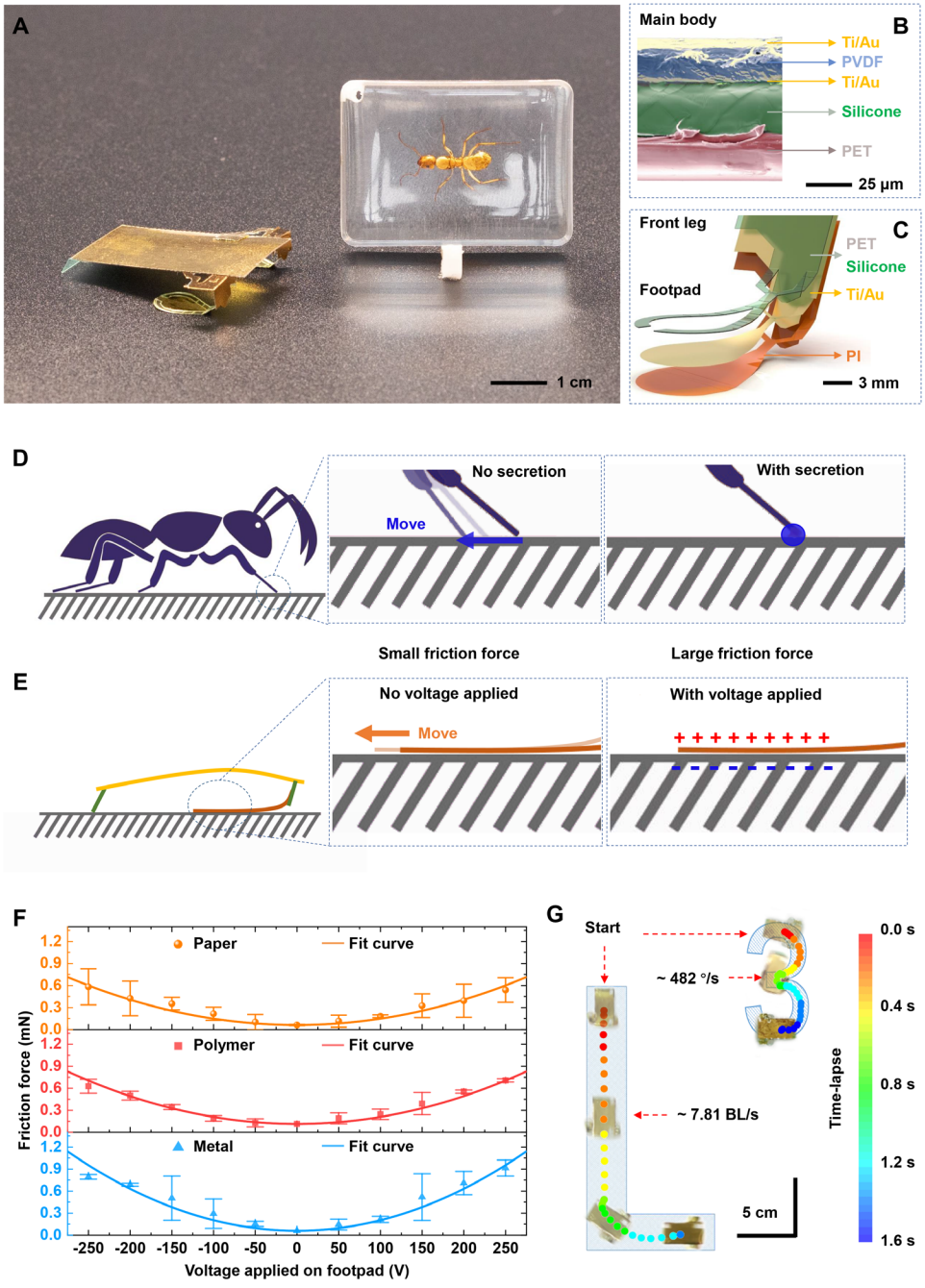

Fig. 1. The design strategy and basic working mechanism. (**A**) An optical image depicting a tethered soft robot of ultrahigh agility with good trajectory manipulation together with a queen ant (*C. turkestanus*). (**B**) Cross-sectional SEM image of the main robot body. (**C**) Schematic diagram showing the structure of an electrostatic footpad. (**D**) Illustration of an ant changing the friction force with a secretion between its foot and ground. (**E**) Illustration of the soft robot changing the friction force with the ground by applying a DC bias voltage between the electrostatic footpad and ground to generate the electrostatic force. (**F**) Measured friction force between the electrostatic footpad of the robot on paper, polymer, and metal substrates under applied DC bias voltages from −250 to 250 V. Error bars represent SD of the friction force calculated from five experiments. (**G**) Demonstration of a tethered soft robot to follow the L and 3 paths at high speeds to illustrate its high agility with good trajectory manipulations.

where $E_{drive}(t)$ and $E_{bias}(t)$ are the electric fields between the electrostatic footpad and substrate from the applied AC driving voltage and DC bias voltage, respectively. Analytically, the main body contracts and extends after the applied AC voltages between the top and bottom electrodes without being affected by the DC bias voltage. On the other hand, the total voltage applied on the footpad is the combination of the AC voltage applied on the main body and the DC bias voltage to generate the asymmetric friction effects on the left and right footpads to regulate the turning motions. Although it is possible to add more electrical wires to independently connect and regulate the body and footpads, this two-wire scheme reduces the complexity of the wiring setup and power electronics.

Figure 2 (B to D) shows the applied AC voltage in one cycle and different DC bias voltages of zero, positive, and negative values for one cycle to produce straight, right turn, and left turn motions, respectively. Under a zero DC bias voltage, the robot moves straight forward because the friction force on the right and left footpads are equal during the first-half period (body extension when the bottom electrode is under a positive voltage via the blue electrical line) and the second-half period (body contraction when the top electrode is under a positive voltage via the orange electrical line). The electrostatic footpad design will not slow down the moving speed when compared with those of soft robots without footpads in the previous work (*18*), which is important to achieve the high agility. Specifically, for a 3-cm-long robot in the previous work, the moving speed was 1.33 BL/s (*18*), and under the same 200-Vpp (peak-to-peak voltage) driving voltage, this work achieves 1.65 BL/s (fig. S6A). Under a positive DC bias voltage and in the first-half period of the AC driving voltage, a higher voltage (AC + DC bias) and friction force will be acting on the right electrostatic footpad when compared with the voltage (AC − DC bias) and resulting friction force acting on the left electrostatic footpad. As such, the right footpad becomes a pivot point due to a high friction force, and the extension of the robot body will induce a net clockwise torque in this period. In the second-half period, the robot is under contraction, and a higher absolute voltage magnitude of "AC − DC bias" and friction force will be acting on the left electrostatic footpad as compared with the absolute voltage magnitude of "AC + DC bias" and resulting friction force acting on the right electrostatic footpad. The left footpad now becomes a

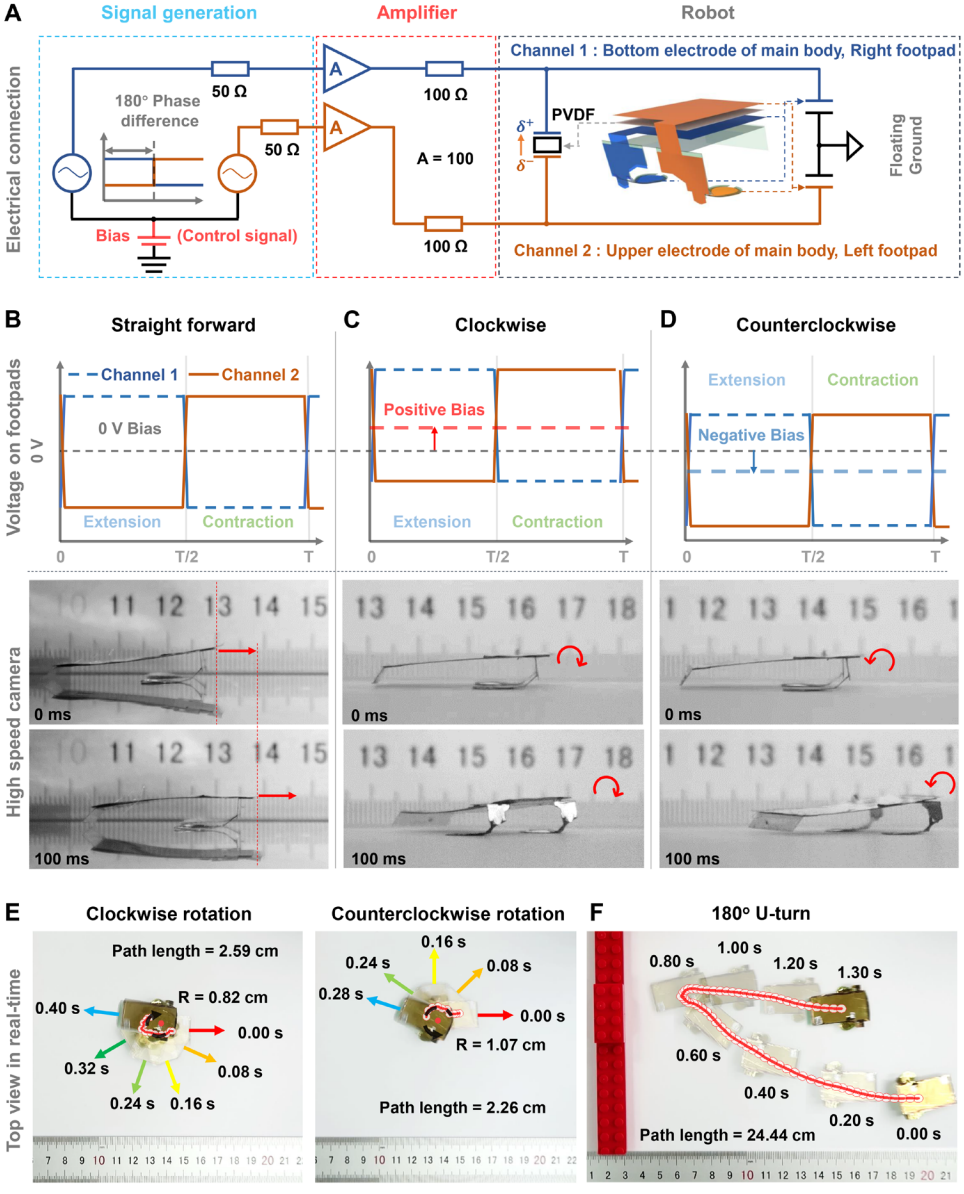

Fig. 2. Trajectory adjustment strategy. (**A**) Schematic diagram of the locomotion adjustment scheme with three key elements: the signal generation module, amplifier module, and robot. The top electrode of the unimorph robot body is connected to the left electrostatic front footpad (orange color), and the bottom electrode of the unimorph robot body is connected to the right electrostatic front footpad (blue color). The turning motion adjustments for (**B**) straight, (**C**) clockwise (right turn), and (**D**) counterclockwise (left turn) motions, respectively, for one cycle of different voltage adjustment schemes (top images), with experimental results within a period of 100 ms (bottom images). (**E**) A clockwise rotation in 0.4 s with a small turning radius of 0.82 cm and a counterclockwise rotation in 0.28 s with a small turning radius of 1.07 cm. (**F**) A 180° "U" turn in 1.3 s.

pivot point with a high friction force, and the contraction of the robot body will induce a net clockwise torque in this period. In other words, both periods will produce clockwise rotation. Conversely, under a negative DC bias voltage, a counterclockwise motion will be generated. An analytical model has been established in the Supplementary Materials with numerical simulations to analyze these turning motions (figs. S9 to S11) together with high-speed camera images and videos by a setup in fig. S3. The details of straight (movie S1), right turn (movie S2), and left turn (movie S3) motions of a tethered prototype in a time scale of 100 ms are summarized in the bottom images in Fig. 2 (B to D), respectively. Testing results for longer operation periods have also been recorded, such as straight forward movements for 13.5 cm in 0.6 s with a relative speed of about 7.5 BL/s (fig. S4A and movie S4), and 90° right and left turns with a radius of 9.1 and 8.8 cm in 0.6 s (fig. S4B/movie S5 and fig. S4C/movie S6), respectively. Several tests have also been conducted on the paper substrate to demonstrate the high agility of the prototype robots with Vpp = 500 V for (i) clockwise and counterclockwise rotations in 0.4 and 0.28 s, with a radius/path of only 0.82 cm/2.59 cm and 1.07 cm/2.26 cm, respectively, in Fig. 2E (movies S7 and S8) and (ii) a 180° U-turn in 1.3 s with a path length of 24.4 cm in Fig. 2F (movie S9).

Turning characterization and design optimization

The DC bias voltage and friction coefficient between the footpad and substrate (fig. S2B) can affect the turning performances. Under three different peak-to-peak AC driving voltages (Vpp = 200, 350, and 500 V), we have systematically measured the turning radius (fig. S5) and relative linear moving speed (fig. S6) of a prototype robot versus footpad DC bias voltages from −250 to 250 V as well as the relative linear velocity versus turning radius (fig. S7). The optical images of a prototype robot on paper, polymer, and metal substrates are shown in fig. S8. As the magnitude of the DC bias voltage increases, the turning agility of the robot increases with reduced turning radius as expected. The metal substrate induces the strongest electrostatic force and the highest friction force to have the smallest turning radius under high absolute DC bias voltages. On the other hand, high AC driving voltages induce large deformations of the robot body to result in fast linear moving speeds, which also contributes to high agility. A figure-of-merit parameter, relative centripetal acceleration (a_r), is adopted to evaluate the turning agility quantitatively

$$a_r = \frac{V^2}{R}\frac{1}{BL} \quad (6)$$

where V is the absolute running speed, R is the turning radius, and BL is the body length of the robot. The unit of the relative centripetal

acceleration is BL/s^2, and a larger value corresponds to better agility. For the three tested substrates, the relative centripetal accelerations under positive and negative DC bias voltages are roughly symmetric with small deviations due to manufacturing variations (Fig. 3, A to C). In general, a high AC driving voltage and a high absolute DC bias voltage are preferred to induce a high relative centripetal acceleration. The high AC voltage will result in a high linear moving speed and high relative centripetal acceleration, as observed in Eq. 6. The high absolute DC bias voltage will result in a large friction force and a reduction in the turning radius to result in a high relative centripetal acceleration. However, if the applied AC driving voltage is low (such as Vpp = 200 or 350 V) and the DC bias voltage is high (such as 250 V), then the relatively small robot body deformations from the low AC driving voltages may not overcome the high electrostatic attraction force on the footpads, and the turning motion is severely reduced to result in low relative centripetal acceleration as shown in the testing results. In the present setup, the highest relative centripetal acceleration was achieved for a tethered prototype at 28 ± 14 BL/s^2 under Vpp = 500 V and a DC bias voltage = −250 V on the metal substrate.

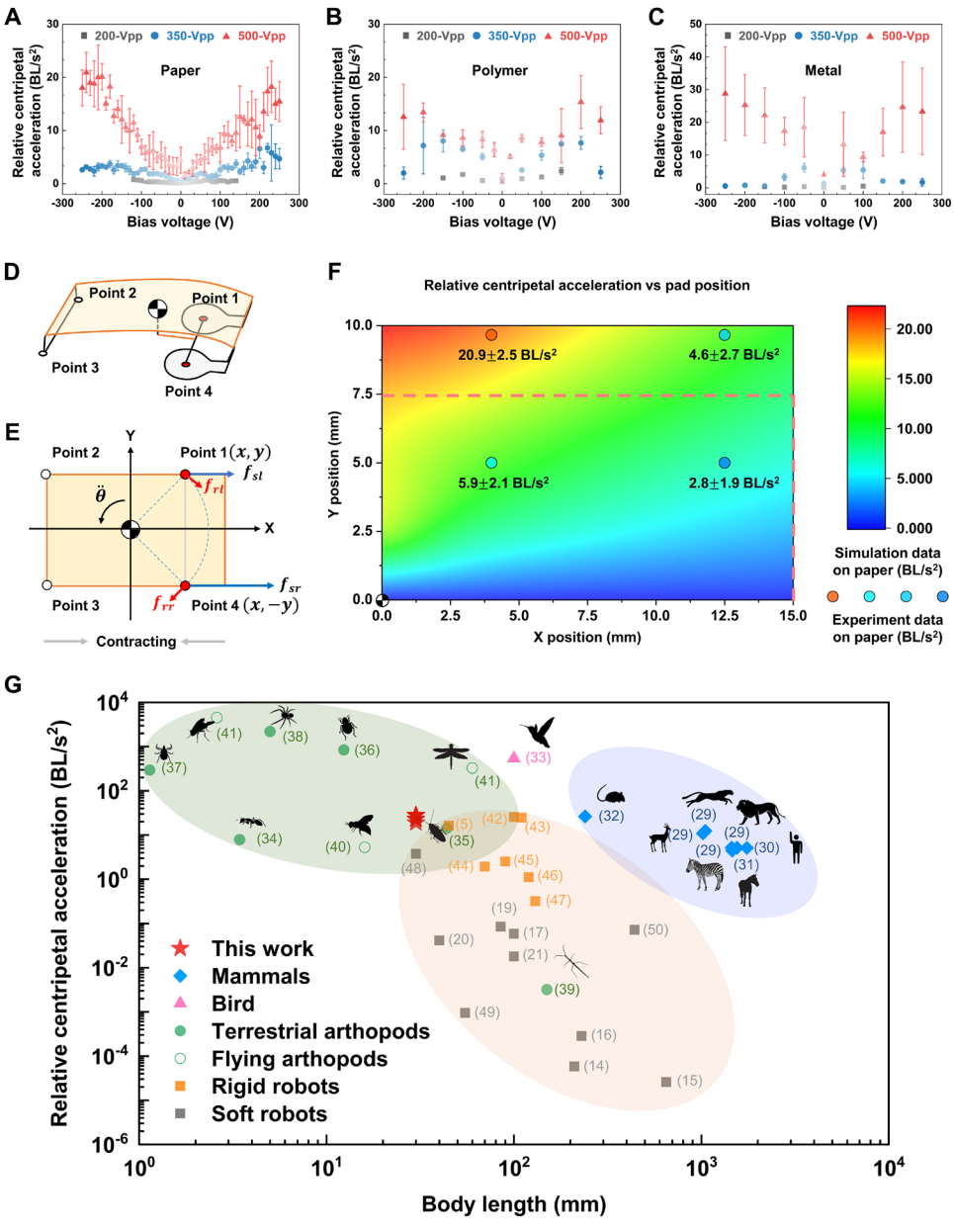

Fig. 3. Turning performances on various substrates and footpad location studies. Relative centripetal acceleration versus applied footpad DC bias voltage on (**A**) paper, (**B**) polymer, and (**C**) metal substrates, under AC driving voltages, Vpp = 200, 350, and 500 V at the resonant frequencies of the tethered prototype robots and applied DC bias voltages between −250 to 250 V. Error bars represent SD of the relative centripetal acceleration calculated from five experiments. (**D**) Simplified dorsal plane model of a robot. (**E**) Location parameters for the electrostatic footpads. (**F**) Simulation and experimental results on the paper substrate for the relative centripetal acceleration and electrostatic footpad locations. (**G**) Relative centripetal accelerations of mammals (blue) (*29–32*), hummingbirds (pink) (*33*), terrestrial arthropods (solid green) (*34–39*), flying arthropods (hollow green) (*40, 41*), rigid robots (orange) (*5, 42–47*), soft robots (gray) (*14–17, 19–21, 48–50*), and this work (red stars) versus body length.

Structural designs also affect the relative centripetal acceleration of the robot, and the locations of the footpads have been investigated as indicated as points 1 and 4 in Fig. 3 (D and E), where x and y represent the distance of the footpads to the center of gravity of the robot body in the x-y coordinate system, respectively. The simulation and experimental results for the relative centripetal acceleration under various combinations of x and y values are shown in Fig. 3F (the detailed simulation setup is explained in the Supplementary Materials). The combination of small x and large y values leads to high relative centripetal acceleration. Qualitatively, the contraction and extension motions of the piezoelectric film can result in a force mainly in the x direction due to the curved piezoelectric film design. For example, if the body is in the contraction mode and the robot is in the counterclockwise motion in Fig. 3E (Fig. 2D for the contraction mode), the footpad at point 4 will have a higher DC bias voltage and higher electrostatic force compared with those at point 1. This results in a higher friction force (f_{sr}) on point 4 in the positive x direction as compared with that on point 1 (f_{sl}) to generate a net counterclockwise steering torque (T_s) as

$$T_s = (f_{sr} - f_{sl}) \times y \qquad (7)$$

This explains that a large y value will generate a large net torque by keeping the same values for all other parameters in favor of a high relative centripetal acceleration. On the other hand, there are tangential forces due to the rotation

movements of the robot at points 1 (f_{rl}) and 4 (f_{rr}) in Fig. 3E, which generate a clockwise resistance torque (T_r) as

$$T_r = (f_{rl} + f_{rr}) \times \sqrt{x^2 + y^2} \quad (8)$$

Here, a small x value will reduce this negative (clockwise) torque in favor of a high relative centripetal acceleration in the counterclockwise direction by keeping the same values for all other parameters. This analysis is based on a small-sized body assumption such that it is not valid for very long robot legs (more than 4 mm) and large values of x and y (more than half of the robot's body length). Experimentally, front footpads with four different locations have been designed and tested. The prototype robot with x and y values of 4.0 and 9.7 mm has the best relative centripetal acceleration of 20.9 ± 2.5 BL/s^2 on the paper substrate, and the experimental results match well with the simulation predictions.

On the basis of the same model, the size of the electrostatic footpad was also analyzed and simulated as shown in fig. S12. In general, the electrostatic force is roughly linearly proportional to the area of the footpad. For footpads with a small radius (such as 0.8 mm), the electrostatic force is too small to induce rotational motions. For footpads with a large radius (such as 4.8 mm), the electrostatic force is too strong, which can reduce the linear running speed of the robot severely. In both cases, the relative centripetal acceleration becomes very small. As such, the footpad size in the prototype robot is chosen to have a radius of 3.2 mm for high relative centripetal accelerations.

Animals with high agility tend to have an advantage in the wild (*29*). A large relative centripetal acceleration means that a robot can run fast and finish a tight turn in a short time. Figure 3G shows the comparison of relative centripetal acceleration with respect to body length for several mammals (blue) (*29*–*32*), hummingbirds (pink) (*33*), terrestrial arthropods (solid green) (*34*–*39*), flying arthropods (hollow green) (*40*, *41*), rigid robots (orange) (*5*, *42*–*47*), soft robots (gray) (*14*–*17*, *19*–*21*, *48*–*50*), and this work (red stars). In general, the relative centripetal acceleration reduces as the body size increases due to the increase of inertia effects, which prevent large objects from making quick turns with a small radius when running at high speeds. Several rigid-body robots have demonstrated high agility in the literature, but it is very challenging for soft robots (as shown in this figure) due to the slow running speeds in most published works. This work has increased the relative centripetal acceleration at least one order of magnitude higher than those of state-of-art soft robots. The difficulty in achieving high agility is to have both high linear moving speed and rotational speed. Specifically, a subject with a high linear moving speed may lose the controllability during the simultaneous turning operations due to the inertia effect. It could be even more challenging for soft robots to achieve high agility without differential gaits (*5*) to realize turning motions due to their low structural stiffness. This work demonstrates the highest relative centripetal accelerations of 28 BL/s^2 among robots due to the combination of several factors: (i) small size and light weight, (ii) strong friction force generated by the electrostatic footpads, and (iii) high linear moving speeds. We provide a short video clip (movie S10) for the turning motions of a cheetah and our soft robot for the ultrahigh agility demonstration and comparison.

Performance and application demonstrations

To test the robustness of the robot, a box that is 200 times heavier (12.9 g) than the weight of the prototype robot was designed to fall from 50 cm above the ground to hit the tethered robot in Fig. 4A (movie S11). The robot was crushed and flattened by the box but recovered quickly afterward in just 40 ms. Although the moving direction of the robot in this case was changed, the relative speed after the crash remained at 7.7 BL/s without degradation. Moreover, after stepping on a prototype robot with a weight of 55.3 kg by a volunteer, the robot kept its turning and running capabilities with excellent robustness, as shown in fig. S13 and movie S12. Another test shows that the robot could pass small obstacles by climbing a 2.4-mm-high step, which is around half of the height of the robot, in 0.29 s, as shown in Fig. 4B (movie S13).

Electrical signals with specific sequences have been manually applied to adjust the moving trajectory of a tethered prototype robot to pass through a 51.2 cm–by–51.2 cm maze, as shown in Fig. 4C (movie S14). A total of 13 continuous motion changes within a total running time of only 5.6 s and a total route length of 120 cm have been achieved in this demonstration. The process was recorded with different colors to illustrate the timing of different turning commands on the right side of the figure. Here, the response time of the electrostatic force, which was used to realize the turning motions of the robot, is ultrafast.

A commercial 180-mg gas sensor (TVOC MiCS-5524, SGX), which is about 2.8 times heavier than the robot, was added to the prototype robot to execute a gas leakage detecting mission, and the detailed design and measurement schemes are given in fig. S14. The tethered robot could move at a speed of 7.6 and 1.2 BL/s under Vpp = 500 V at the resonant frequency of 143 and 111 Hz without and with the gas sensor, respectively. As indicated in Fig. 4D and movie S15, there was a designated ethanol gas leakage spot in a pipe made of LEGO bricks. The robot carrying the gas sensor could complete a designed route with nine temporary stops (60 s at each stop point) to record a gas concentration route map. The maximum recorded concentration was 3869 parts per million at point 6, which was in front of the ethanol leakage point. The slightly high concentrations at the starting point and before the ethanol leakage spot are due to the airflow direction and leaks from the LEGO constructions. These testing results illustrate key capabilities of the soft robots for potential practical applications, including, but not limited to, attaching gas sensors for hazardous gas detections and attaching other sensors and cameras for sensing and surveillance functions.

Untethered operations

An untethered version of the soft robot (2.4 cm by 2.2 cm, 240 mg) together with a payload of 1.66 g—including a battery (3.7 V, 40 mAh; HuiXinLi Inc.), two photo sensors (GL3549, JCGL Inc.), and a flexible circuit board—was constructed to demonstrate the trajectory manipulation and power autonomy, as illustrated in Fig. 5A. The measured resonance frequency was 410 Hz with several slightly different design alternations compared with that of the tethered robot for better operations, including (i) the PVDF poling direction changed from top to bottom, (ii) a PI frame added to the front of the robot to carry the two photoresistors and support the front loads, and (iii) two PI supporting structures added to increase the loading capacity, as shown in Fig. 5B. If the center of gravity of the robot moves closer to the head position, then the linear moving velocity of the robot increases (fig. S15A). On the other hand, the linear moving speed of the robot decreases as the payload increases as expected (fig. S15B). Specifically, a prototype without carrying any payload had a linear moving velocity of 3.4 BL/s. The speed decreased to

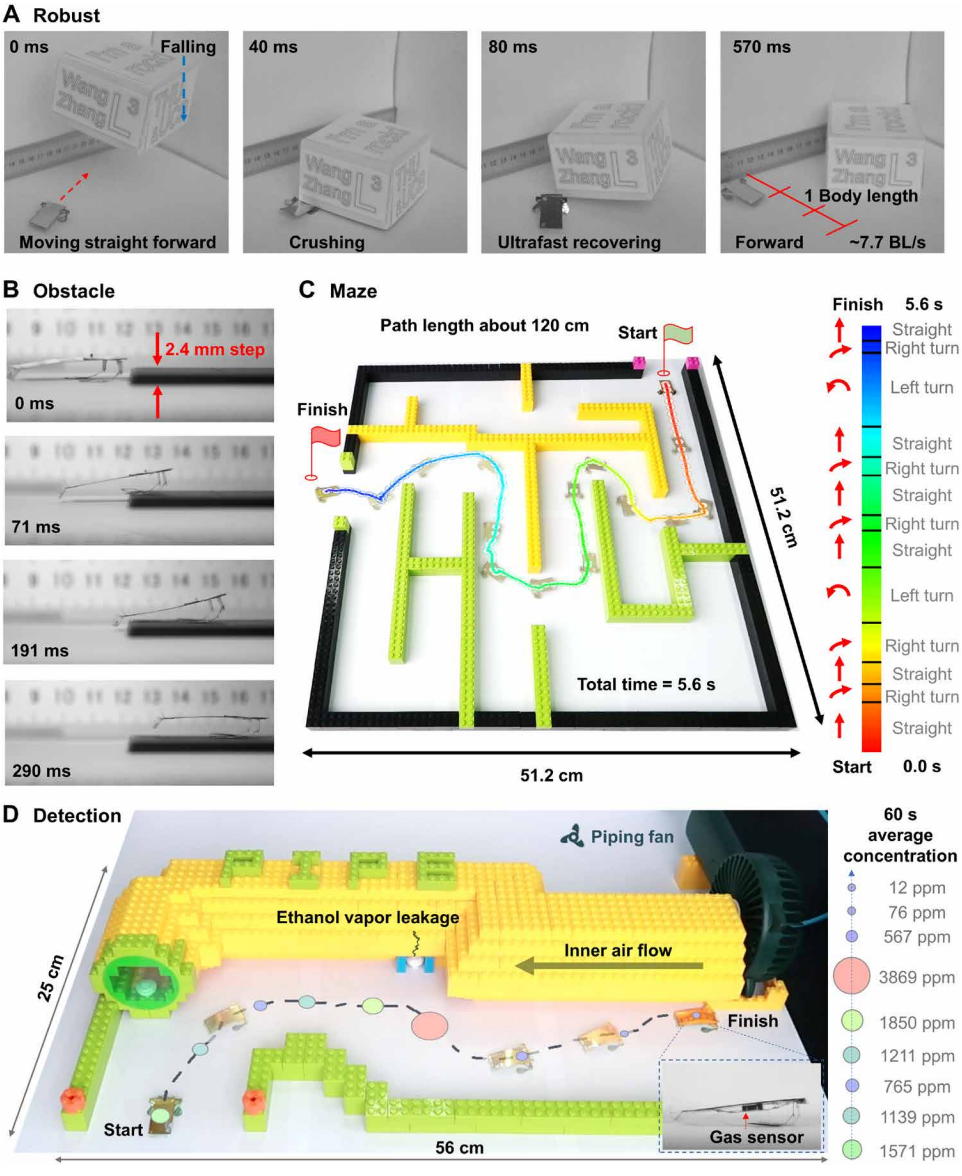

Fig. 4. Performance and application demonstrations for a tethered prototype robot. (**A**) Robustness demonstration. A 200 times heavier box falling on the robot from 50 cm above the ground shows that the robot has the ability of quick recovery to make normal forward movements. (**B**) The robot climbed an obstacle with a step height of 2.4 mm. (**C**) A tethered prototype robot rapidly passed through a maze in only 5.6 s. (**D**) A tethered prototype robot carrying an ethanol gas sensor for a leakage detection mission recorded the concentration route map. Inset: The cross-sectional view of the robot carrying a gas sensor.

1.2 BL/s under the payload of 1.66 g (movie S16) and further decreased to 0.4 BL/s with a payload of 2.5 g. Inspired by the antennae navigation and photophobia behavior of insects (*51*, *52*), two photoresistors were used to realize the turning function of the robot with an analog control scheme (*53*) as illustrated in Fig. 5C, with a detailed circuit diagram in fig. S16A. Specifically, the circuit can output a 500-Vpp driving voltage to the robot's main body with the left/right photoresistors connected to the top electrode of the main body and the right/left footpads, respectively. A footpad can be treated as a capacitor and is connected in series with a photoresistor. The voltage amplitude-frequency response on the footpad can be calculated as

$$A(\omega) = \frac{1}{\sqrt{1 + (\omega RC)^2}} \quad (9)$$

where ω is the driving frequency, R is the resistance of the photoresistor, and C is the capacitance of the footpad. A large resistance value of the photoresistor will result in a low voltage on the footpad. Under a laser beam, the photoresistor's resistance drops from 170 to 2 kilohms, which can be used to regulate the applied voltages on the footpads. Specifically, when a laser is pointing at the left/right photoresistor, a 500-Vpp voltage is applied to generate the electrostatic force on the right/left footpads for the right/left turns, respectively. Figure 5E and movie S16 show one manipulation example of this scheme to realize a designated S-shaped path on a paper substrate to include straight, left turn (5.6°/s at a radius of 10.5 cm), and right turn (10.2°/s at a radius of 6.4 cm) motions. The total time is 36.9 s for the robot to complete a 27.9-cm-long path. In the endurance test (fig. S16B), the untethered robot could move for a distance of 31 m in 19 min, which corresponds to an average speed of 27.2 mm/s, an average power consumption of 397 mW, a cost of transport (COT) of 887 with a driving circuit efficiency of 11.8%, and a relative centripetal acceleration of 0.09 BL/s^2. In comparison, the running speed of a previously reported insect-scale soft robot with a payload of 780 mg (including electronics and battery components) was 12 mm/s with a COT of 1670, a driving circuit efficiency of 7.5%, and a relative centripetal acceleration at 0.04 BL/s^2 (*20*). Most insect-scale robots, such as legged robots and flying robots (*20*, *54*–*56*), have used digital control schemes for manipulations and operations. This work used the analog control scheme for simple operational controls, and possible further weight reductions by using lightweight components could lead to more efficient operations.

CONCLUSION

By regulating the friction force of the two electrostatic footpads with a simple scheme via two electrical wires with the combination of AC and DC bias voltages, an insect-scale tethered soft robot with excellent robustness achieved both high moving speeds and turning capabilities for ultrahigh agility and trajectory manipulations. The resulting relative centripetal acceleration of 28 BL/s^2 is the highest among all small soft robots, which is comparable or better than

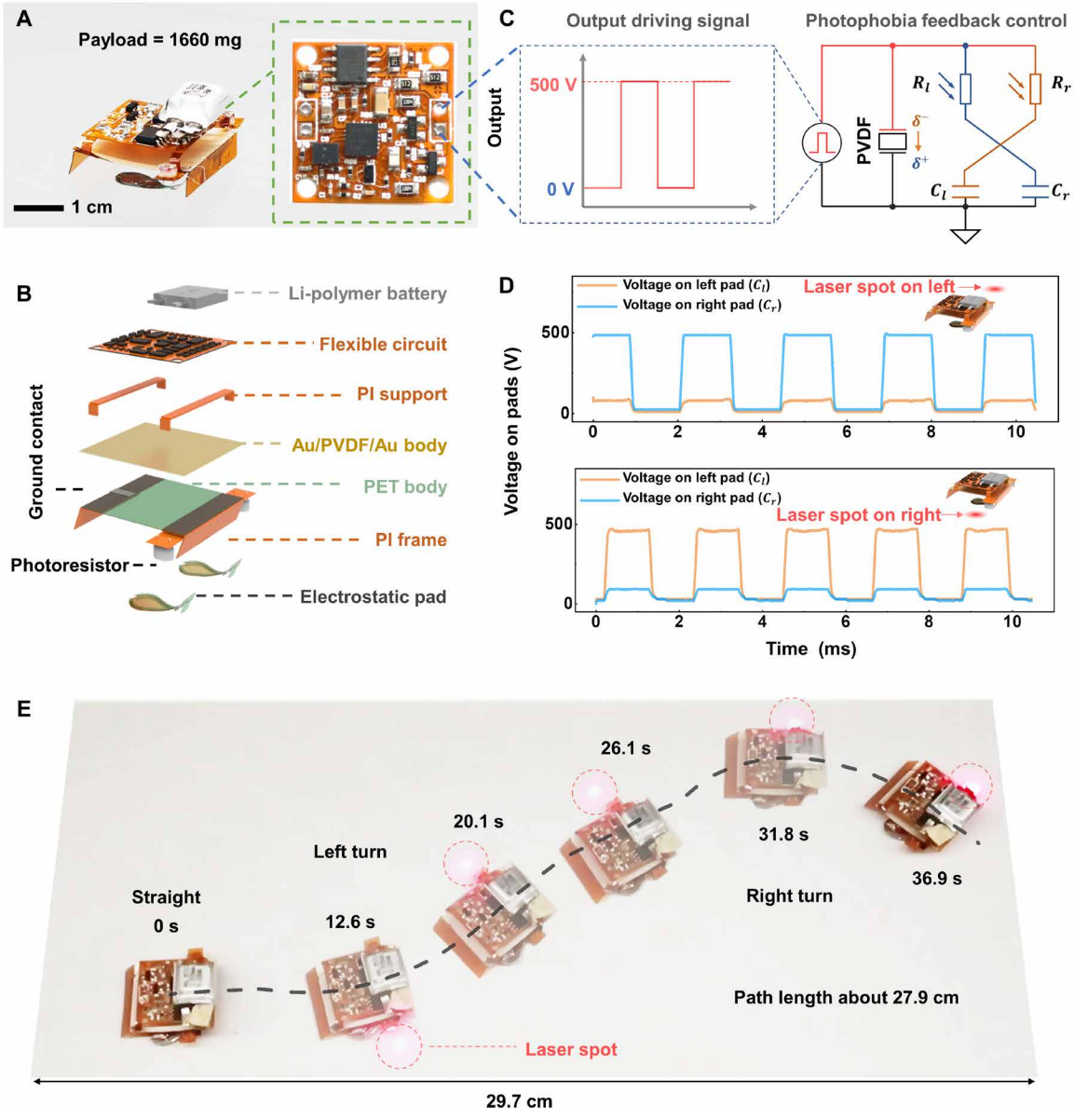

Fig. 5. Design and performances of an untethered soft robot. (**A**) An optical photo of an untethered soft robot with a battery, photoresistors, and a flexible circuit (a total weight of 1.66 g). Inset: The flexible circuit. (**B**) Schematic diagram illustrating the design and assembly of the untethered robot. (**C**) The output driving signal from the control circuit with photoresistors. (**D**) Measured voltage on the left and right footpads when a laser is irradiating at the left (top) and right (bottom) photoresistors, respectively. (**E**) Trajectory manipulation demonstration of an untethered robot to complete a 27.9-cm-long, S-shaped path on a paper substrate in 36.9 s with the combination of straight, left, and right turn motions adjusted by a laser.

many terrestrial arthropods, such as the cockroach. By carrying a commercial gas sensor, an ethanol leakage detection mission was successfully demonstrated by the tethered soft robot. The study on the relative centripetal acceleration versus body length for the state-of-the-art works from living insects, mammals, and robots has shown that miniaturization is favorable for achieving high agility. The simplified turning regulation scheme helps to reduce the complexity of powering electronics for the construction of an untethered soft robot by integrating a battery, two photosensors, and a flexible circuit. A laser pointer has been used to adjust the left/right turns of the robot as an example toward practical applications. Some possible future directions and challenges include (i) miniaturizations to further increase the agility; (ii) new design, material, and mechanism to improve the motion trajectory control and increase the payload capacity; (iii) sensors and mechanisms for autonomous feedback controls with speedy responses; (iv) wireless communication systems with low-latency wireless link for information exchanges; and (v) on-board energy storage or conversion devices for sustainable long-term operations. These and other supporting efforts could eventually lead to the performance improvements of insect-scale soft robots to match agile insects for the execution of practical and important tasks in various applications.

MATERIALS AND METHODS

Design and fabrication of the robot

Main body structure fabrication (18)

A 18-μm-thick and 3 cm–by–1.5 cm PVDF (PolyK Technologies LLC) film was first deposited with 10-nm-thick Ti and 100-nm-thick Au films on both sides by the electron beam evaporation process. The Ti layer enhanced the bonding strength between the Au and PVDF. A 25-μm-thick PET film (Gizmo Dorks) with a 25-μm-thick sticky silicone layer was prestretched by first removing the protection layer. One side of the PET film was clamped, and the other side was connected to a force gauge on a Thorlabs translational stage. With the applied force of 1 ± 0.2 Newton, the 3 cm–by–1.5 cm PET film was carefully stretched along the length direction, and the PVDF film was attached and laminated with the silicone adhesion layer, as shown in Fig. 6A. A curved robot body was fabricated with a measured curvature of 2.13 ± 0.16 m^{-1} for five samples.

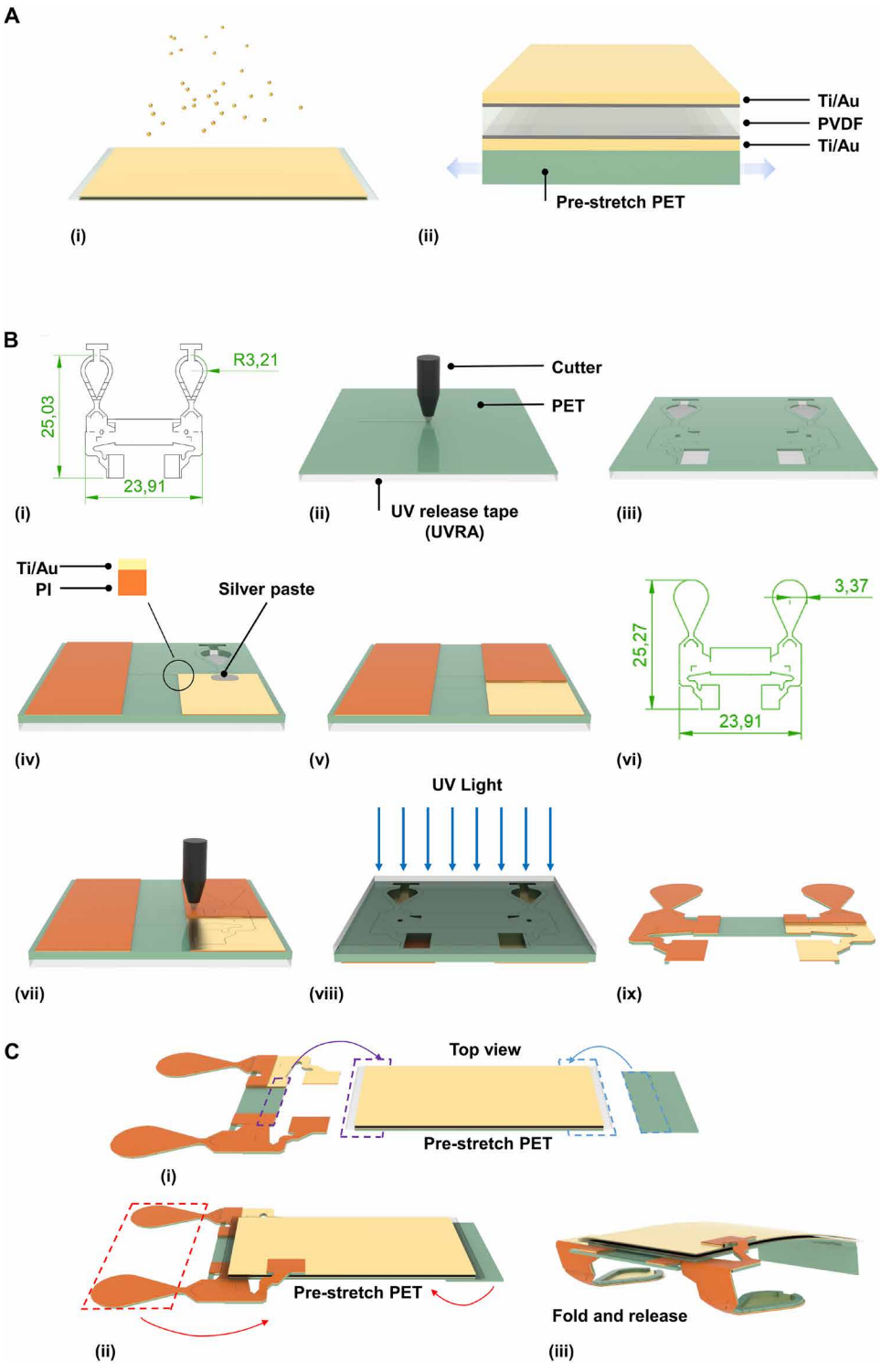

Fig. 6. The fabrication process for the soft robot. (**A**) The unimorph robot body, (**B**) the front legs, and (**C**) final assembly.

Front legs and footpad fabrication

The front legs and footpads were composed of 25-μm-thick PET film with a 25-μm-thick sticky silicone layer and a 5-μm-thick PI film (DuPont) with 10-nm-thick Ti/100-nm-thick Au films as the electrode. The front structures are fabricated by a vinyl cutter (Cameo 3, Silhouette) with the leg height of 4 mm and a footpad area of 32 mm^2, as shown in Fig. 6Bi. The structure of the front footpad was defined by the vinyl cutter to cut out the unused portion of the PET film while keeping the bottom 25-μm-thick ultraviolet (UV) release tape (YL-150PO, Carfort), shown as Fig. 6Bii. The unused portion of the upper PET layer was cut and removed to construct the supporting structure (Fig. 6Biii). For the left-side region of the leg and footpad, the PI/Ti/Au electrode film was laminated on the sticky silicone by exposing the PI film. For the right-side region, the leg area was laminated with the PI/Ti/Au electrode film by exposing the Ti/Au film, whereas the joint area was covered with silver paste (DJ-002, MCN) to ensure good conductivity. The footpad area was laminated with the PI/Ti/Au electrode film by exposing the PI film (Fig. 6B, iv and v). The physical outline of the front leg and footpads was patterned and cut by the vinyl cutter (Fig. 6B, vi and vii). The as-fabricated structure was treated with 365-nm UV light for 20 min to reduce the viscosity of the UV release tape (Fig. 6Bviii). Last, the structure, including the front legs and footpads, was peeled off from the UV release tape (UVRA, YL-150PO, Carfort). (Fig. 6Bix).

Rear leg fabrication

The PET layer was patterned and cut with the vinyl cutter to define the rear

leg structure with a folding crease. The height of the rear leg was 3.5 mm after the folding process.

Assembly

The front legs and footpads and the rear leg were laminated to the main body structure by the sticky silicone layer on the PET film, as shown in Fig. 6Ci. The upper electrode of the PVDF main body was connected to the left front footpad, and the bottom electrode of the PVDF main body was connected to the right front footpad. The front footpads and rear leg were folded about 90° and 70°, respectively (Fig. 6Cii). Two 18-μm-diameter silver wires were connected to the upper and bottom electrodes to provide electrical power. The assembled robot is shown in the schematic diagram (Fig. 6Ciii).

SUPPLEMENTARY MATERIALS

robotics.sciencemag.org/cgi/content/full/6/55/eabe7906/DC1
Sections S1 to S9
Figs. S1 to S16
Tables S1 to S4
Movies S1 to S16
References (*57*, *58*)

REFERENCES AND NOTES

1. N. W. Bartlett, M. T. Tolley, J. T. B. Overvelde, J. C. Weaver, B. Mosadegh, K. Bertoldi, G. M. Whitesides, R. J. Wood, A 3D-printed, functionally graded soft robot powered by combustion. *Science* **349**, 161–165 (2015).
2. Y. Kim, H. Yuk, R. Zhao, S. A. Chester, X. Zhao, Printing ferromagnetic domains for untethered fast-transforming soft materials. *Nature* **558**, 274–279 (2018).
3. H. Arazoe, D. Miyajima, K. Akaike, F. Araoka, E. Sato, T. Hikima, M. Kawamoto, T. Aida, An autonomous actuator driven by fluctuations in ambient humidity. *Nat. Mater.* **15**, 1084–1089 (2016).
4. W. Hu, G. Z. Lum, M. Mastrangeli, M. Sitti, Small-scale soft-bodied robot with multimodal locomotion. *Nature* **554**, 81–85 (2018).
5. B. Goldberg, N. Doshi, R. J. Wood, High speed trajectory control using an experimental maneuverability model for an insect-scale legged robot, in *2017 IEEE International Conference on Robotics and Automation (ICRA)* (IEEE 2017), Singapore, Singapore, 29 May to 3 June 2017.
6. A. T. Baisch, C. Heimlich, M. Karpelson, R. J. Wood, HAMR3: An autonomous 1.7 g ambulatory robot, in *2011 IEEE/RSJ International Conference on Intelligent Robots and Systems* (IEEE 2011), San Francisco, CA, USA, 25 to 30 September 2011.
7. S. D. de Rivaz, B. Goldberg, N. Doshi, K. Jayaram, J. Zhou, R. J. Wood, Inverted and vertical climbing of a quadrupedal microrobot using electroadhesion. *Sci. Robot.* **3**, eaau3038 (2018).
8. A. T. Baisch, O. Ozcan, B. Goldberg, D. Ithier, R. J. Wood, High speed locomotion for a quadrupedal microrobot. *Int. J. Rob. Res.* **33**, 1063–1082 (2014).
9. J. E. Clark, J. G. Cham, S. A. Bailey, E. M. Froehlich, P. K. Nahata, R. J. Full, M. R. Cutkosky, Biomimetic design and fabrication of a hexapedal running robot, in *Proceedings 2001 ICRA. IEEE International Conference on Robotics and Automation (cat. no. 01CH37164)* (IEEE 2001), Seoul, South Korea, South Korea, 21 to 26 May 2001.
10. P. Birkmeyer, K. Peterson, R. S. Fearing, DASH: A dynamic 16g hexapedal robot, in *2009 IEEE/RSJ International Conference on Intelligent Robots and Systems* (IEEE 2009), St. Louis, MO, USA, 10 to 15 October 2009.
11. Y. Yang, Z. Pei, Z. Li, Y. Wei, Y. Ji, Making and remaking dynamic 3D structures by shining light on flat liquid crystalline vitrimer films without a mold. *J. Am. Chem. Soc.* **138**, 2118–2121 (2016).
12. R. F. Shepherd, F. Ilievski, W. Choi, S. A. Morin, A. A. Stokes, A. D. Mazzeo, X. Chen, M. Wang, G. M. Whitesides, Multigait soft robot. *Proc. Natl. Acad. Sci. U.S.A.* **108**, 20400–20403 (2011).
13. S. Miyashita, S. Guitron, S. Li, D. Rus, Robotic metamorphosis by origami exoskeletons. *Sci. Robot.* **2**, eaao4369 (2017).
14. T. Duggan, L. Horowitz, A. Ulug, E. Baker, K. Petersen, Inchworm-inspired locomotion in untethered soft robots, in *2019 2nd IEEE International Conference on Soft Robotics (RoboSoft)* (IEEE 2019), Seoul, Korea (South), Korea (South), 14 to 18 April 2019.
15. M. T. Tolley, R. F. Shepherd, B. Mosadegh, K. C. Galloway, M. Wehner, M. Karpelson, R. J. Wood, G. M. Whitesides, A resilient, untethered soft robot. *Soft Robot.* **1**, 213–223 (2014).
16. Y. O. Aydin, J. L. Molnar, D. I. Goldman, F. L. Hammond, Design of a soft robophysical earthworm model, in *2018 IEEE International Conference on Soft Robotics (RoboSoft)* (IEEE 2018), Livorno, Italy, 24 to 28 April 2018.
17. Z. Zhang, X. Wang, S. Wang, D. Meng, B. Liang, Design and modeling of a parallel-pipe-crawling pneumatic soft robot. *IEEE Access* **7**, 134301–134317 (2019).
18. Y. Wu, J. K. Yim, J. Liang, Z. Shao, M. Qi, J. Zhong, Z. Luo, X. Yan, M. Zhang, X. Wang, R. S. Fearing, R. J. Full, L. Lin, Insect-scale fast moving and ultrarobust soft robot. *Sci. Robot.* **4**, eaax1594 (2019).
19. G. Gu, J. Zou, R. Zhao, X. Zhao, X. Zhu, Soft wall-climbing robots. *Sci. Robot.* **3**, eaat2874 (2018).
20. X. Ji, X. Liu, V. Cacucciolo, M. Imboden, Y. Civet, A. El Haitami, S. Cantin, Y. Perriard, H. Shea, An autonomous untethered fast soft robotic insect driven by low-voltage dielectric elastomer actuators. *Sci. Robot.* **4**, eaaz6451 (2019).
21. C. Tang, B. Li, H. Chen, U-turning an agile robotic cube by a soft dielectric elastomer resonator, in *2018 IEEE International Conference on Soft Robotics (RoboSoft)* (IEEE 2018), Livorno, Italy, 24 to 28 April 2018.
22. Y. Chen, H. Zhao, J. Mao, P. Chirarattananon, E. F. Helbling, N.-s. P. Hyun, D. R. Clarke, R. J. Wood, Controlled flight of a microrobot powered by soft artificial muscles. *Nature* **575**, 324–329 (2019).
23. W. Federle, M. Riehle, A. S. Curtis, R. J. Full, An integrative study of insect adhesion: Mechanics and wet adhesion of pretarsal pads in ants. *Integr. Comp. Biol.* **42**, 1100–1106 (2002).
24. W. Federle, W. Baumgartner, B. Hölldobler, Biomechanics of ant adhesive pads: Frictional forces are rate- and temperature-dependent. *J. Exp. Biol.* **207**, 67–74 (2004).
25. P. Drechsler, W. Federle, Biomechanics of smooth adhesive pads in insects: Influence of tarsal secretion on attachment performance. *J. Comp. Physiol. A Neuroethol. Sens. Neural Behav. Physiol.* **192**, 1213–1222 (2006).
26. W. Federle, D. Labonte, Dynamic biological adhesion: Mechanisms for controlling attachment during locomotion. *Philos. Trans. R. Soc. Lond. B Biol. Sci.* **374**, 20190199 (2019).
27. D. Labonte, W. Federle, Rate-dependence of 'wet' biological adhesives and the function of the pad secretion in insects. *Soft Matter* **11**, 8661–8673 (2015).
28. D. Labonte, W. Federle, Scaling and biomechanics of surface attachment in climbing animals. *Philos. Trans. R. Soc. Lond. B Biol. Sci.* **370**, 20140027 (2015).
29. A. M. Wilson, T. Y. Hubel, S. D. Wilshin, J. C. Lowe, M. Lorenc, O. P. Dewhirst, H. L. A. Bartlam-Brooks, R. Diack, E. Bennitt, K. A. Golabek, Biomechanics of predator–prey arms race in lion, zebra, cheetah and impala. *Nature* **554**, 183–188 (2018).
30. Y.-H. Chang, R. Kram, Limitations to maximum running speed on flat curves. *J. Exp. Biol.* **210**, 971–982 (2007).
31. H. Tan, A. M. Wilson, Grip and limb force limits to turning performance in competition horses. *Proc. R. Soc. B* **278**, 2105–2111 (2011).
32. R. M. Walter, Kinematics of 90 running turns in wild mice. *J. Exp. Biol.* **206**, 1739–1749 (2003).
33. P. S. Segre, R. Dakin, V. B. Zordan, M. H. Dickinson, A. D. Straw, D. L. Altshuler, Burst muscle performance predicts the speed, acceleration, and turning performance of Anna's hummingbirds. *eLife* **4**, e11159 (2015).
34. J. M. C. Pearce-Duvet, C. P. H. Elemans, D. H. Feener Jr., Walking the line: Search behavior and foraging success in ant species. *Behav. Ecol.* **22**, 501–509 (2011).
35. D. L. Jindrich, R. J. Full, Many-legged maneuverability: Dynamics of turning in hexapods. *J. Exp. Biol.* **202**, 1603–1623 (1999).
36. F. E. Fish, A. J. Nicastro, Aquatic turning performance by the whirligig beetle: Constraints on maneuverability by a rigid biological system. *J. Exp. Biol.* **206**, 1649–1656 (2003).
37. S. Rubin, M. H.-Y. Young, J. C. Wright, D. L. Whitaker, A. N. Ahn, Exceptional running and turning performance in a mite. *J. Exp. Biol.* **219**, 676–685 (2016).
38. Y. Zeng, S. Crews, Biomechanics of omnidirectional strikes in flat spiders. *J. Exp. Biol.* **221**, jeb166512 (2018).
39. V. Dürr, W. Ebeling, The behavioural transition from straight to curve walking: Kinetics of leg movement parameters and the initiation of turning. *J. Exp. Biol.* **208**, 2237–2252 (2005).
40. V. Zolotov, L. Frantsevich, E.-M. Falk, Kinematik der phototaktischen Drehung bei der Honigbiene*Apis mellifera* L. *J. Comp. Physiol.* **97**, 339–353 (1975).
41. S. A. Combes, D. E. Rundle, J. M. Iwasaki, J. D. Crall, Linking biomechanics and ecology through predator–prey interactions: Flight performance of dragonflies and their prey. *J. Exp. Biol.* **215**, 903–913 (2012).
42. N. J. Kohut, A. O. Pullin, D. W. Haldane, D. Zarrouk, R. S. Fearing, Precise dynamic turning of a 10 cm legged robot on a low friction surface using a tail, in *2013 IEEE International Conference on Robotics and Automation* (IEEE 2013), Karlsruhe, Germany, 6 to 10 May 2013.
43. C. Casarez, I. Penskiy, S. Bergbreiter, Using an inertial tail for rapid turns on a miniature legged robot, in *2013 IEEE International Conference on Robotics and Automation* (IEEE 2013), Karlsruhe, Germany, 6 to 10 May 2013.
44. H. Peng, T. Mao, X. Lu, A small legged deformable robot with multi-mode motion. *J. Intell. Mater. Syst. Struct.* **31**, 704–718 (2020).

45. H. H. Hariri, G. S. Soh, S. Foong, K. L. Wood, A highly manoeuvrable and untethered under-actuated legged piezoelectric miniature robot, in *International Design Engineering Technical Conferences and Computers and Information in Engineering Conference (ASME 2019)*, Anaheim, California, USA, 18 to 21 August 2019.
46. D. Zarrouk, R. S. Fearing, Controlled in-plane locomotion of a hexapod using a single actuator. *IEEE Trans. Robot.* **31**, 157–167 (2015).
47. M. P. Murphy, M. Sitti, Waalbot: An agile small-scale wall-climbing robot utilizing dry elastomer adhesives. *IEEE ASME Trans. Mechatron.* **12**, 330–338 (2007).
48. J. Liang, Y. Wu, Z. Shao, J. K. Yim, R. Xu, Y. Song, M. Qi, J. Zhong, M. Zhang, X. Wang, Manipulating the moving trajectory of insect-scale piezoelectric soft robots by frequency, in *2019 IEEE 32nd International Conference on Micro Electro Mechanical Systems (MEMS)* (IEEE 2019), Seoul, Korea (South), 27 to 31 Jan. 2019.
49. J. Bao, W. Chen, J. Xu, Kinematics modeling of a twisted and coiled polymer-based elastomer soft robot. *IEEE Access* **7**, 136792–136800 (2019).
50. C. M. Donatelli, Z. T. Serlin, P. Echols-Jones, A. E. Scibelli, A. Cohen, J.-M. Musca, S. Rozen-Levy, D. Buckingham, R. White, B. A. Trimmer, Soft foam robot with caterpillar-inspired gait regimes for terrestrial locomotion, in *2017 IEEE/RSJ International Conference on Intelligent Robots and Systems (IROS)* (IEEE 2017), Vancouver, BC, Canada, 24 to 28 September 2017.
51. N. J. Cowan, J. Lee, R. J. Full, Task-level control of rapid wall following in the American cockroach. *J. Exp. Biol.* **209**, 1617–1629 (2006).
52. R. B. Zajonc, A. Heingartner, E. M. Herman, Social enhancement and impairment of performance in the cockroach. *J. Pers. Soc. Psychol.* **13**, 83–92 (1969).
53. V. Braitenberg, *Vehicles: Experiments in Synthetic Psychology* (MIT Press, 1986).
54. N. T. Jafferis, E. F. Helbling, M. Karpelson, R. J. Wood, Untethered flight of an insect-sized flapping-wing microscale aerial vehicle. *Nature* **570**, 491–495 (2019).
55. B. Goldberg, R. Zufferey, N. Doshi, E. F. Helbling, G. Whittredge, M. Kovac, R. J. Wood, Power and control autonomy for high-speed locomotion with an insect-scale legged robot. *IEEE Robot. Autom. Let.* **3**, 987–993 (2018).
56. V. Iyer, A. Najafi, J. James, S. Fuller, S. Gollakota, Wireless steerable vision for live insects and insect-scale robots. *Sci. Robot.* **5**, eabb0839 (2020).
57. C.-H. Hsueh, Modeling of elastic deformation of multilayers due to residual stresses and external bending. *J. Appl. Phys.* **91**, 9652–9656 (2002).
58. T. L. Hedrick, Software techniques for two- and three-dimensional kinematic measurements of biological and biomimetic systems. *Bioinspir. Biomim.* **3**, 034001 (2008).

Acknowledgments: We thank HuiXinLi Inc. for providing the battery. We thank S. Tang for image processing and R. Xu for suggestions on fabrication methods. **Funding:** This work is supported by the Natural Science Foundation of Guangdong Province (2020A1515010647), Shenzhen Fundamental Research Funds (JCYJ20180508151910775), the National Natural Science Foundation of China (grant no. 52005083), and Start Research Grant from University of Macau. J. L. is supported by a scholarship from TBSI. **Author contributions:** J.L. designed the prototypes and setups, performed the experiments, and wrote the paper. Y.W. designed the prototypes and assisted fabrication. J.K.Y. assisted the simulations. H.C., H.L., and Z.M. assisted the experiments. Ying L., Yixin L., D.W., W.Q., and Z.S. interpreted the data. X.W. commented the paper. M.Z., J.Z., and L.L. directed the research and revised the paper. **Competing interests:** M.Z., J.L., Y.W., and X.W. are inventors on patent application (201910288596.2) submitted by Shenzhen International Graduate School, Tsinghua University that covers the principle and structure of robot turning. The other authors declare that they have no competing interests. **Data and materials availability:** All data needed to evaluate the conclusions are available in the paper or the Supplementary Materials.

Submitted 14 September 2020
Accepted 2 June 2021
Published 30 June 2021
10.1126/scirobotics.abe7906

Citation: J. Liang, Y. Wu, J. K. Yim, H. Chen, Z. Miao, H. Liu, Y. Liu, Y. Liu, D. Wang, W. Qiu, Z. Shao, M. Zhang, X. Wang, J. Zhong, L. Lin, Electrostatic footpads enable agile insect-scale soft robots with trajectory control. *Sci. Robot.* **6**, eabe7906 (2021).

Science Robotics

Electrostatic footpads enable agile insect-scale soft robots with trajectory control

Jiaming Liang, Yichuan Wu, Justin K. Yim, Huimin Chen, Zicong Miao, Hanxiao Liu, Ying Liu, Yixin Liu, Dongkai Wang, Wenying Qiu, Zhichun Shao, Min Zhang, Xiaohao Wang, Junwen Zhong, and Liwei Lin

Sci. Robot. **6** (55), eabe7906. DOI: 10.1126/scirobotics.abe7906

Science Robotics (ISSN 2470-9476) is published by the American Association for the Advancement of Science. 1200 New York Avenue NW, Washington, DC 20005. The title *Science Robotics* is a registered trademark of AAAS.